

# New aerosol models for the retrieval of aerosol optical thickness and normalized water-leaving radiances from the SeaWiFS and MODIS sensors over coastal regions and open oceans

Ziauddin Ahmad,<sup>1,2,\*</sup> Bryan A. Franz,<sup>1</sup> Charles R. McClain,<sup>1</sup> Ewa J. Kwiatkowska,<sup>1,3</sup> Jeremy Werdell,<sup>1,4</sup> Eric P. Shettle,<sup>5</sup> and Brent N. Holben<sup>1</sup>

<sup>1</sup>NASA Goddard Space Flight Center, Greenbelt Road, Greenbelt, Maryland 20771, USA

<sup>2</sup>Science and Data Systems, Inc., 16509 Copperstrip Lane, Silver Spring, Maryland 20906, USA

<sup>3</sup>Science Applications International Corporation, 10260 Campus Point Drive, San Diego, California, 92121, USA

<sup>4</sup>Science Systems and Application, Inc., 10210 Greenbelt Road, Lanham Maryland 20706, USA

<sup>5</sup>Naval Research Laboratory, Washington, D.C. 20375, USA

\*Corresponding author: Ziauddin.Ahmad@nasa.gov

Received 18 February 2010; revised 20 July 2010; accepted 26 August 2010;  
posted 7 September 2010 (Doc. ID 124415); published 5 October 2010

We describe the development of a new suite of aerosol models for the retrieval of atmospheric and oceanic optical properties from the SeaWiFS and MODIS sensors, including aerosol optical thickness ( $\tau$ ), angstrom coefficient ( $\alpha$ ), and water-leaving radiance ( $L_w$ ). The new aerosol models are derived from Aerosol Robotic Network (AERONET) observations and have bimodal lognormal distributions that are narrower than previous models used by the Ocean Biology Processing Group. We analyzed AERONET data over open ocean and coastal regions and found that the seasonal variability in the modal radii, particularly in the coastal region, was related to the relative humidity. These findings were incorporated into the models by making the modal radii, as well as the refractive indices, explicitly dependent on relative humidity. From these findings, we constructed a new suite of aerosol models. We considered eight relative humidity values (30%, 50%, 70%, 75%, 80%, 85%, 90%, and 95%) and, for each relative humidity value, we constructed ten distributions by varying the fine-mode fraction from zero to 1. In all, 80 distributions ( $8Rh \times 10$  fine-mode fractions) were created to process the satellite data. We also assumed that the coarse-mode particles were nonabsorbing (sea salt) and that all observed absorptions were entirely due to fine-mode particles. The composition of the fine mode was varied to ensure that the new models exhibited the same spectral dependence of single scattering albedo as observed in the AERONET data. The reprocessing of the SeaWiFS data show that, over deep ocean, the average  $\tau_{865}$  values retrieved from the new aerosol models was  $0.100 \pm 0.004$ , which was closer to the average AERONET value of  $0.086 \pm 0.066$  for  $\tau_{870}$  for the eight open-ocean sites used in this study. The average  $\tau_{865}$  value from the old models was  $0.131 \pm 0.005$ . The comparison of monthly mean aerosol optical thickness retrieved from the SeaWiFS sensor with AERONET data over Bermuda and Wallops Island show very good agreement with one another. In fact, 81% of the data points over Bermuda and 78% of the data points over Wallops Island fall within an uncertainty of  $\pm 0.02$  in optical thickness. As a part of the reprocessing effort of the SeaWiFS data, we also revised the vicarious calibration gain factors, which resulted in significant improvement in angstrom coefficient ( $\alpha$ ) retrievals. The average value of  $\alpha$  from the new models over Bermuda is  $0.841 \pm 0.171$ , which is in good agreement with the AERONET value of  $0.891 \pm 0.211$ . The average value of  $\alpha$  retrieved using old models is  $0.394 \pm 0.087$ , which is significantly lower than the AERONET value. © 2010 Optical Society of America

OCIS codes: 070.4550, 070.6110, 120.5050, 120.6650.

## 1. Introduction

One of the most challenging tasks in satellite remote sensing of the oceans is to accurately quantify the phytoplankton abundance, colored dissolved organic matter (CDOM), and inherent optical properties of the water column. These quantities are determined from the spectral distribution of water-leaving radiances ( $L_w$ ) at the ocean surface, which are only a small fraction of the downwelling solar irradiance that is backscattered to the top of the atmosphere (TOA) by subsurface constituents of the ocean. Under ideal conditions of clear water in the deep ocean (depth > 1000 m),  $L_w$  in the blue part of the spectrum is only about 10%–15% of the total radiance at the TOA, which is mostly dominated by Rayleigh and Mie scattering by air molecules and aerosols, respectively, in the atmosphere. In coastal areas like Chesapeake Bay, the contribution of  $L_w$  to TOA radiance may decrease to less than 5% due to an increase in absorption by chlorophyll and CDOM in the water column. Hence, to accurately retrieve the water-leaving radiance and derive bio-optical properties of the ocean from satellite remote sensing data, an accurate determination of the atmospheric contribution to TOA radiance, also known as atmospheric correction, is required.

Although the physics of the scattering by air molecules and aerosols is well understood, the accuracy of atmospheric correction is dependent on the determination of microphysical and optical properties (e.g., size distribution and complex index of refraction) of aerosols that, unfortunately, are temporally and spatially variant in concentration and particle type. The different types of atmospheric aerosols observed over oceans and their origins are discussed in the review article by Husar *et al.* [1] and references therein. They are briefly summarized as follows. Over open oceans, where maritime influences dominate, aerosols are generally nonabsorbing and mainly consist of sea salt and water produced from the breakup of water bubbles. In addition to these naturally occurring aerosols, there are anthropogenic aerosols, such as sulfates produced by industries and transported across the North Atlantic and North Pacific Oceans. Similarly, there are smoke aerosols that are produced from biomass burning in Western Africa and Central America. Sulfate aerosols are nonabsorbing, whereas smoke shows strong absorption, particularly in the red part of the spectrum. Another strongly absorbing aerosol found over the Atlantic Ocean is Saharan dust, which originates from Western Africa and is transported across the Central Atlantic to North and Central America. Likewise, aerosols originating from the Gobi desert cross the Western Pacific Ocean and are often observed over the continental United States of America. Both the Saharan and Gobi dust aerosols are more absorbing in the blue than in the red part of the spectrum.

Aerosols are often classified into groups based on their origin. For example, Shettle and Fenn [2] (here-

after SF79) broadly divide the aerosols into two main groups: continental and maritime aerosols, and further subdivide the continental aerosols into rural and urban origins and maritime aerosols into oceanic and continental origins. d'Almeida *et al.* [3] provide a more comprehensive classification of aerosols for the purpose of climate studies. In particular, they divide maritime aerosols into three subcategories: clean maritime, maritime mineral, and maritime polluted. They define the clean-maritime aerosols as consisting of sea salt and non-sea-salt-sulfate (NSS) aerosols found in remote areas of oceans, maritime-mineral aerosols as consisting of desert dust and aerosols of maritime origin, and maritime-polluted aerosols as consisting of crustal, anthropogenic aerosols transported through continental air mass and aerosols of maritime in origin.

Over the past several decades, many attempts have been made to describe the size distribution of aerosols through analytical functions. Based on field measurements, Junge [4] proposed a power-law function, and Deirmendjian [5,6] suggested use of a modified gamma function to describe the size distribution of aerosols. Deirmendjian also showed that the modified gamma function correctly describes the polarization properties of aerosols and water clouds. Later, Davies [7] reported that Junge's power law does not accurately account for large particles in observed size distributions, and proposed a lognormal function to describe the size distribution of aerosols. Based on his work, it is now customary to assume lognormal distribution for aerosol size distribution. Also, compared to Deirmendjian's modified gamma distribution, the constants of the lognormal distribution are more intuitive. Another interesting feature of the lognormal distribution is that each component of the distribution has a unique modal radius, standard deviation, and refractive index, and can be traced to its source or origin. In their classification of aerosols, both SF79 and d'Almeida *et al.* [3] assumed lognormal distributions to describe the aerosols in the atmosphere.

To process large amounts of satellite data from sensors like SeaWiFS, Gordon and Wang [8] (hereafter GW94), and Gordon [9] used SF 79's lognormal distributions of tropospheric and maritime aerosols and proposed a suite of aerosol models to estimate atmospheric correction. They constructed these distributions to represent tropospheric, coastal, maritime, and oceanic aerosols. Their tropospheric and oceanic models were identical to SF79's lognormal models for tropospheric and maritime aerosols, whereas their maritime and coastal aerosol models were bi-modal lognormal models constructed by combining 99% (99.5%) of SF79 tropospheric and 1% (0.5%) of maritime aerosols, by number of particles, respectively. It should be noted that these aerosol models do not represent smoke or Saharan dust over the ocean. Antoine and Morel [10] used similar aerosol models to process MERIS data; however, their suite of operational models also includes dust models. They refer

to their models as marine, urban, continental, and dust aerosols models. The former two are derived from SF79's models, and the latter two are taken from World Climate Radiation Program [11], and from measurements reported by Schütz [12]. Both GW94 and Antoine and Morel account for the effect of relative humidity on the aerosols' microphysical and optical properties. They use the variation of the mean geometric radius and refractive index of aerosols with relative humidity from SF79, which was based on the data of Hänel [13].

With development of the AERONET program by NASA in the late 1990s, a large database of sunphotometer derived aerosol properties, including optical thickness and size distributions over land and oceanic sites, are now available to investigators for scientific research. Using AERONET data, Smirnov *et al.* [14] reported aerosol size distributions over open oceans that are quite different from GW94's maritime aerosol models. For example, GW94's maritime aerosol model for relative humidity of 90% has modal radii (standard deviation) values for fine and coarse modes in volume size distribution space as 0.274 (0.806) and 4.842 (0.921)  $\mu\text{m}$ , respectively; whereas, Smirnov's average values for fine and coarse modes for the Lanai, Nauru, and Tahiti sites in the Pacific Ocean from the most recent processing of the AERONET data are 0.177 (0.477) and 2.555 (0.678), respectively. If we add two other sites in Smirnov's paper, namely, Bermuda and Ascension Island, then the average values for the fine and coarse modes become 0.171 (0.460) and 2.503 (0.676), respectively. In other words, AERONET aerosol size distributions derived from maritime locations are narrower than GW94's.

A few years ago, Wang *et al.* [15] analyzed the SeaWiFS derived atmospheric and oceanic data products produced by the Ocean Biology Processing Group (OBPG) and concluded that, although, the water-leaving radiances were in good agreement with the *in situ* measurements, the retrieved aerosol products (optical thickness and angstrom coefficient) differed significantly from the AERONET measurements. They also reported that GW94's models often overestimate atmospheric correction in the coastal region, particularly over the Eastern U.S., where the water-leaving radiance retrieval in the blue channel (412 nm) of the SeaWiFS and MODIS sensors is sometimes negative.

In this paper, we describe the details of an effort to develop a new set of aerosol models to improve the quality of the atmospheric correction and retrieved aerosol properties from SeaWiFS and MODIS sensors. These models are designed to span the range of aerosol size distributions and optical properties observed at maritime AERONET sites, including both open-ocean and coastal environments. For information on the open ocean, we focus on a suite of AERONET sites located on small islands away from major land masses. For the coastal environment, the Chesapeake Bay Region (CBR) serves as a useful proxy, as it spans a wide range of water types from

highly turbid in the northern extent to nearly oceanic in the south, with aerosol influences from industrial cities, suburban areas, agricultural land use, and the Atlantic Ocean. The CBR is also well equipped with three long-standing AERONET stations and an ongoing water-quality monitoring program.

We incorporate the models developed from these AERONET observations into the global processing chain within the OBPG, and show how they significantly improve the agreement of retrieved aerosol properties from SeaWiFS relative to *in situ* measurements. We also explore the impact of this improved aerosol retrieval on the quality of atmospheric correction and water-leaving radiance retrievals. The aerosol models developed through this work will ultimately be applied to the reproduction of all operational ocean color products distributed by NASA from the SeaWiFS and MODIS sensors. This is the first effort to update the operational aerosol models since the original atmospheric correction approach for SeaWiFS was developed by GW94 in the early 1990s.

## 2. AERONET Data

### A. Background

The details of AERONET network and measurements are described in many papers, including Holben *et al.* [16,17], Dubovik and King [18], Dubovik *et al.* [19–22] and Sinyuk *et al.* [23]. Briefly, AERONET data consist of optical thickness and microphysical parameters of aerosols in the atmosphere. The optical thickness is derived from the direct measurements of the Sun in eight spectral bands centered at 340, 380, 440, 500, 670, 940, and 1020 nm, and microphysical properties, such as aerosol size distribution, are derived from diffuse sky radiance measurements, generally in four bands at 440, 670, 870, and 1020 nm along the principal plane and along the solar almucantar. The principal plane measurements are carried out by varying the zenith angle at a fixed azimuth angle and the solar almucantar by varying the azimuth angle at a constant zenith angle. The aerosol optical thickness is derived from the Beer–Bouguer law, where the contributions from Rayleigh and trace gas optical thicknesses are subtracted from the total optical thickness derived from the slope of the log of irradiance versus path length line. The volume size distribution ( $dV/d(\ln r)$ ) is retrieved in 22 equidistance bins in  $\ln r$  space, where the radius of the particle,  $r$ , varies from 0.05 to 15  $\mu\text{m}$ .

A detailed analysis of the AERONET retrieved aerosol volume size distributions shows that the distributions can be approximated by a sum of two lognormal distributions written as

$$\frac{dV(r)}{d \ln r} = \sum_{i=1}^2 \frac{V_{oi}}{\sqrt{2\pi}\sigma_i} \exp \left[ -\left( \frac{\ln r - \ln r_{voi}}{\sqrt{2}\sigma_i} \right)^2 \right], \quad (1)$$

where  $V_{oi}$  is the volume of the particles,  $r_{voi}$  is the volume geometric mean radius, and  $\sigma_i$  is the

geometric standard deviation. The subscript  $i$  represents the  $i$ th mode of the distribution.

In the number density space, Eq. (1) takes the form

$$\frac{dN(r)}{d \ln r} = \sum_{i=1}^2 \frac{N_{oi}}{\sqrt{2\pi}\sigma_i} \exp \left[ -\left( \frac{\ln r - \ln r_{noi}}{\sqrt{2}\sigma_i} \right)^2 \right], \quad (2)$$

where  $N_{oi}$  is the number of particles, and  $r_{noi}$  is the mean geometric radius of the  $i$ th distribution, and the radius  $r_{noi}$  and  $N_{oi}$  are, respectively, related to  $r_{voi}$  and  $V_{oi}$  as

$$\ln r_{noi} = \ln r_{voi} - 3\sigma_i^2, \quad (3a)$$

$$N_{oi} = V_{oi} [0.75 / (\pi r_{noi}^3)] \exp(-4.5\sigma_i^2). \quad (3b)$$

Two other quantities of interest are effective radius ( $r_{\text{eff}}$ ) and effective variance ( $v_{\text{eff}}$ ), which are defined as

$$r_{\text{eff}} = \int_{r_{\min}}^{r_{\max}} \pi r^3 n(r) dr / \int_{r_{\min}}^{r_{\max}} \pi r^2 n(r) dr, \quad (4a)$$

$$v_{\text{eff}} = \int_{r_{\min}}^{r_{\max}} (r - r_{\text{eff}})^2 \pi r^2 n(r) dr / r_{\text{eff}}^2 \int_{r_{\min}}^{r_{\max}} \pi r^2 n(r) dr, \quad (4b)$$

where

$$n(r) = dN/dr.$$

Hansen and Travis [24] have shown that all distributions (for example, modified gamma, power law, and various lognormal distributions) that have the same values of  $r_{\text{eff}}$  and  $v_{\text{eff}}$  have very similar scattering properties. We use these parameters, particularly effective radius, in discussing the properties of the open-ocean and regional aerosol models described in the following sections.

## B. Aerosol Properties Over Open Oceans and Coastal Regions

### 1. Size Distribution

To understand the characteristics of aerosols over open oceans, we searched the AERONET database and identified 15 sites for the analysis. On further examination we found that many of those sites had limited data records. We selected eight sites that had about 150 or more daily averaged observations. These sites, along with their latitude–longitude and data span, are listed in Table 1 and shown in Fig. 1. Three of these sites (Lanai, Midway, and Tahiti) are in the Pacific Ocean, three (Cape Verde, Ascension Island, and Bermuda) are in the Atlantic Ocean, and the final two (Kaashidhoo and Darwin) are in the Indian Ocean. Although Darwin is a coastal site, here we have treated it as an open-ocean site. It is recognized that some of these sites, such as Cape Verde, may have episodic influx of desert dust or biomass burning aerosols in addition to oceanic aerosols, but the retrievals need to work for those cases, also. We also selected three sites (SERC, Wallops Island, and COVE) over the CBR. These sites cover the upper, middle, and lower regions of Chesapeake Bay. Details of these sites are also listed in Table 1. Also, to ensure compatibility with the operational processing of the satellite data from MODIS and SeaWiFS sensors, where scenes with optical thickness greater than approximately 0.3 are generally masked as clouds, we selected only those measurements where retrieved aerosol optical thickness was less than or equal to 0.3. Finally, to get a better understanding of the aerosol microphysical and optical properties, we converted the daily averaged data into monthly averaged data and examined in detail the seasonal behavior of a few selected parameters, including mean geometric modal radius [in  $dV/d(\ln r)$  space], standard deviations, effective radius, and relative concentration of fine- and coarse-mode particles. We found that, over the open ocean, the monthly mean data of modal radii showed large variations; however, when we constructed the monthly climatology, the large variations disap-

**Table 1. Name and Location of the AERONET Sites and Number of Observations (Daily Averaged) Used for Analysis of Aerosol Size Distribution over Chesapeake Bay and Open Ocean**

Type	Site	Location (Lat., Long.)	Data Record	No. of Observations
Coastal	COVE	36.90N, 75.710W	Oct. 1999–Dec. 2006	740
	Wallops Island	37.942N, 75.475W	Jul. 1993–Aug. 2007	985
	SERC	38.883N, 76.500W	Nov. 1994–Jun. 2006	468
Open ocean	Lanai	20.735N, 156.922W	Nov. 1996–Oct. 2004	678
	Cape Verde	16.733N, 022.935W	Jan. 1996–Apr. 2007	512
	Tahiti	17.577S, 149.606W	Aug. 1999–Oct 2003	247
	Kaashidhoo	04.965N, 073.466E	Feb. 1998–May 2000	149
	Darwin	12.424S, 130.892E	Apr. 2004–Nov. 2005	235
	Ascension Island	07.976S, 014.415W	Dec. 1998–May 2006	293
	Bermuda	32.370N, 064.696W	Apr. 1996–Nov. 2002	192
	Midway Island	28.210N, 177.378W	Jan. 2001–Sep. 2006	237



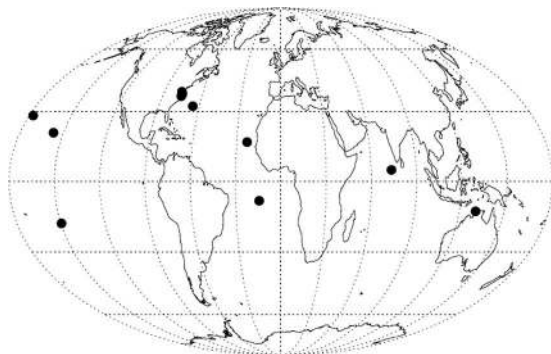


Fig. 1. Locations of oceanic and coastal AERONET sites used in the present study.

peared and there was a relatively smooth variation in the modal radii values with season. Over the CBR, the three sites had very similar variation with season, suggesting that aerosol characteristics over the upper, middle, and lower bay were consistent. Figures 2(a)–2(c) show the monthly climatology of

the mean geometric radius and standard deviation of the fine and coarse modes for both the open-ocean and CBR aerosols. For open ocean, the fine-mode radius monotonically decreases from January to June, shows a bump in the months of July and August, and then increases monotonically from September until December. The maximum value ( $0.177\ \mu\text{m}$ ) occurs in January and the minimum value ( $0.162\ \mu\text{m}$ ) in May, as well as in June. We do not find any discernible seasonal trend in the coarse-mode values. The maximum value ( $2.564\ \mu\text{m}$ ) occurs in December and the minimum value ( $2.279\ \mu\text{m}$ ) in April. Similarly, there is no trend in the standard deviation values of the fine and coarse modes over the open ocean. The maximum value of the standard deviation,  $0.485$  ( $0.676$ ), for the fine (coarse) mode occurs in April (March), while the minimum values of  $0.453$  and  $0.656$ , respectively, for the fine and coarse modes occur in December. For the CBR aerosols, we find that the fine-mode radius is smaller in the months of April and October ( $\sim 0.16\ \mu\text{m}$ ) than in July and August

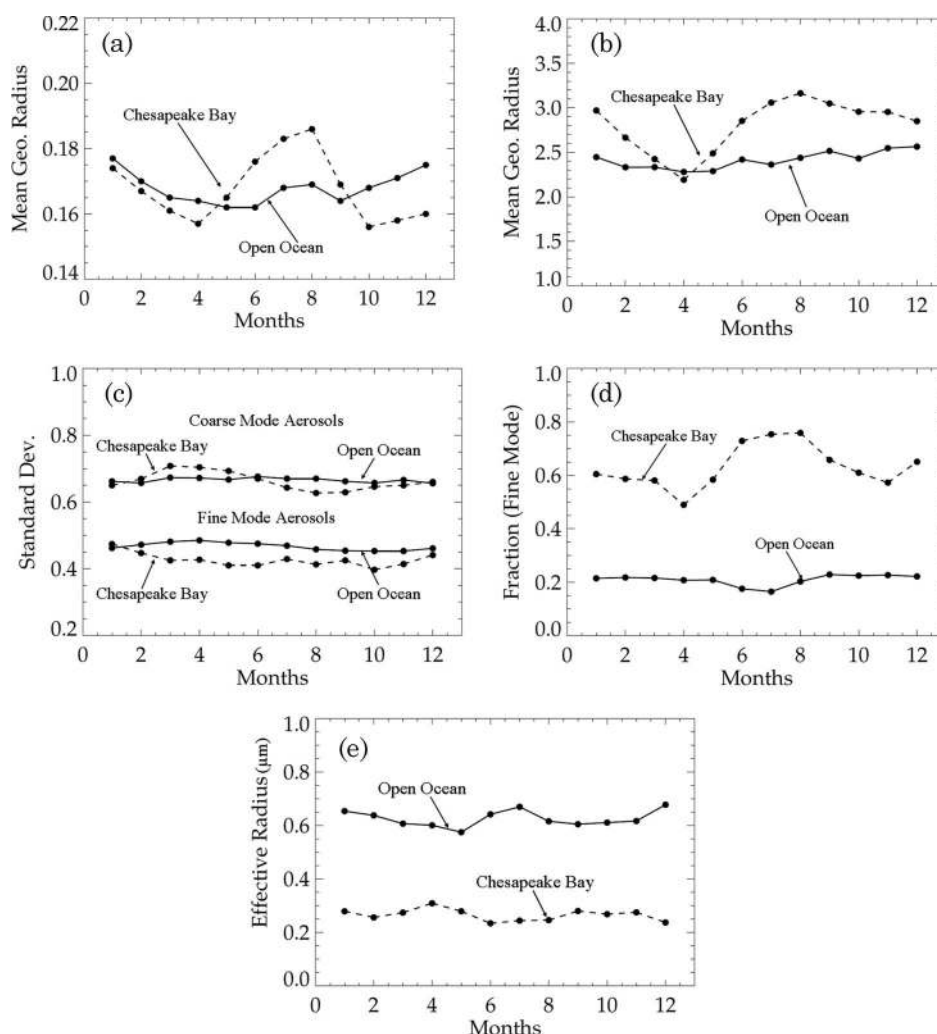


Fig. 2. (a) Monthly mean geometric radius of fine-mode aerosols (in volume distribution space) observed over open ocean and CBR. (b) Same as in (a), but for coarse-mode aerosols. (c) Monthly mean standard deviation of fine- and coarse-mode aerosols over open ocean and the CBR. (d) Monthly mean fraction (by volume) of the fine-mode distributions over open ocean and the CBR. (e) Effective radius of aerosols over open ocean and the CBR.

( $\sim 0.185 \mu\text{m}$ ). The coarse-mode radius shows a minimum value ( $2.3 \mu\text{m}$ ) in the month of April and maximum value ( $3.2 \mu\text{m}$ ) in June, July, and August. Unlike the fine mode, the coarse mode does not show any minimum in September, but it slowly decreases to  $2.9 \mu\text{m}$  in December. With respect to standard deviation, we find that, for the fine mode, the values are slightly greater in January and February ( $\sim 0.46$ ) than in June and October ( $\sim 0.42$ ); whereas, for the coarse mode, the standard deviation value is maximum ( $0.7$ ) in the month of April and minimum ( $\sim 0.615$ ) in the months of August and September.

We also examined the fine-mode fraction [Fig. 2(d)] and found no seasonal trend over the open ocean. The maximum and minimum values were, respectively,  $0.245$  and  $0.182$ , and occurred in September and July. The average value of the fine-mode fraction was  $0.212$ . Over the CBR, we do find a trend in the fine-mode-fraction values. It is significantly higher during the months of June, July, and August ( $0.729$ ,  $0.754$ , and  $0.759$ ) than for other months, for which the value varies from  $0.490$  in April to  $0.658$  in September. The average value of the fine-mode fraction over the CBR is  $0.632$ .

The effective radius shows a weak trend with season [Fig. 2(e)]. Over open ocean, it decreases monotonically from January ( $0.680 \mu\text{m}$ ) to May ( $0.571 \mu\text{m}$ ), shows a sudden increase during the months of June and July ( $0.648 \mu\text{m}$  and  $0.664 \mu\text{m}$ ), and then reaches another minimum ( $0.613 \mu\text{m}$ ) in September. Finally, it slowly reaches to its maximum value ( $0.714 \mu\text{m}$ ) in December. The average value of the effective radius over open ocean is  $0.638 \mu\text{m}$ . Over the Chesapeake Bay, the trend is very weak. It varies from  $0.279 \mu\text{m}$  in January to  $0.309 \mu\text{m}$  in April, and then drops to  $0.234 \mu\text{m}$  in June. Afterward, it fluctuates between  $0.280 \mu\text{m}$  in September and  $0.237 \mu\text{m}$  in December. We find the average value of the effective radius over the CBR to be  $0.265 \mu\text{m}$ , indicating the strong influence of the fine-mode tropospheric aerosols. A summary of the average values of the parameters described above is given in Table 2.

## 2. Single Scattering Albedo

An examination of the single scattering albedo (SSA) data over the open ocean shows that, most of the time, the AERONET stations did not report the SSA values. For the eight open-ocean sites,  $97.1\%$  of the data (2469 daily averaged observations) did

not have any SSA values. We believe that this is mostly due to large uncertainty in the retrieved SSA values when the aerosol optical thicknesses are small ( $< \sim 0.2$ ), which is generally the case over open ocean. For the remaining  $2.9\%$  of the data (74 daily averaged observations), which came from four sites: Cape Verde, Kaashidhoo, Darwin, and Ascension Island, the average value SSA for the  $440 \text{ nm}$  band was  $0.872 \pm 0.051$ . These cases included a significant contribution from dust and/or biomass burning aerosols, in addition to the normal oceanic aerosols.

Over the CBR,  $19.3\%$  of the data (423 daily averaged observations) did not have any SSA value, and only  $5\%$  (110 observations) of the reported data had SSA ( $440 \text{ nm}$ ) values of less than  $0.935$ . The frequency distribution [see Fig. 3(a)] shows a peak around  $0.97$ . Since AERONET assigns a low confidence level to SSA values when aerosol optical thickness at  $870 \text{ nm}$  ( $\tau_{870}$ ) is small (less than  $0.2$ ), we selected data where  $\tau_{870}$  fell between  $0.2$  and  $0.3$  to get a better understanding of SSA values over the CBR. We found that, for the dataset where  $0.2 \leq \tau_{870} \leq 0.3$  and  $\text{SSA} \geq 0.935$ , the SSA was essentially constant ( $0.975$ ) over a six month period from May to October [Fig. 3(b)]. In our dataset, we did not find observations for winter months that would satisfy the optical thickness and SSA criteria stated above. Another quantity of interest was the spectral dependence of the SSA. Saharan dust aerosols have a positive slope in the visible part of the spectrum, whereas maritime-polluted aerosols exhibit negative slope (Dubovik *et al.* [20]). To examine the spectral slope of the SSA in our data, we determined the mean value for each wavelength of the AERONET observations. The result of this exercise is shown in Fig. 3(c), where we find a linear dependence of SSA on wavelength. Here, slope is negative, that is, SSA decreases with an increase in wavelength, indicating that CBR aerosols can be classified as maritime-polluted aerosols. For the open-ocean data, we found only eight observations that would satisfy the optical thickness criteria ( $0.2 \leq \tau_{870} \leq 0.3$ ) and all of them had  $\text{SSA}(440 \text{ nm}) \leq 0.935$ . It appears that most of the absorbing aerosol data over the open ocean were due to smoke and soot, at the four island stations.

While analyzing the data over the CBR and open ocean, we found a linear relationship between the aerosol angstrom coefficient ( $\alpha_{440}$ ), which defines the spectral dependence between  $\tau_{440}$  and  $\tau_{865}$ , and

**Table 2. Average Values of Modal Radii ( $r_{vf}$ ,  $r_{vc}$ ), Standard Deviations ( $\sigma_f$ ,  $\sigma_c$ ), Effective Radius  $r_{\text{eff}}$ , and Fine-Mode Fraction  $f$  for Fine- and Coarse-Mode Aerosols over Open Ocean and Chesapeake Bay<sup>a</sup>**

	Fine Mode			Coarse Mode			$r_{\text{eff}}$	$N$
	$r_{vf}$	$\sigma_f$	$f$	$r_{vc}$	$\sigma_c$	$1 - f$		
Open ocean	0.171	0.462	0.257	2.492	0.678	0.743	0.612	1794
Chesapeake Bay	0.168	0.427	0.629	2.790	0.664	0.371	0.266	2193

<sup>a</sup>The subscripts  $v$ ,  $f$ , and  $c$ , respectively, refer to volume space, fine mode, and coarse mode of the aerosols, and  $N$  in the last column of the table represents the total number of daily averaged observations. (Note: these numbers slightly differ from mean of the monthly average values).

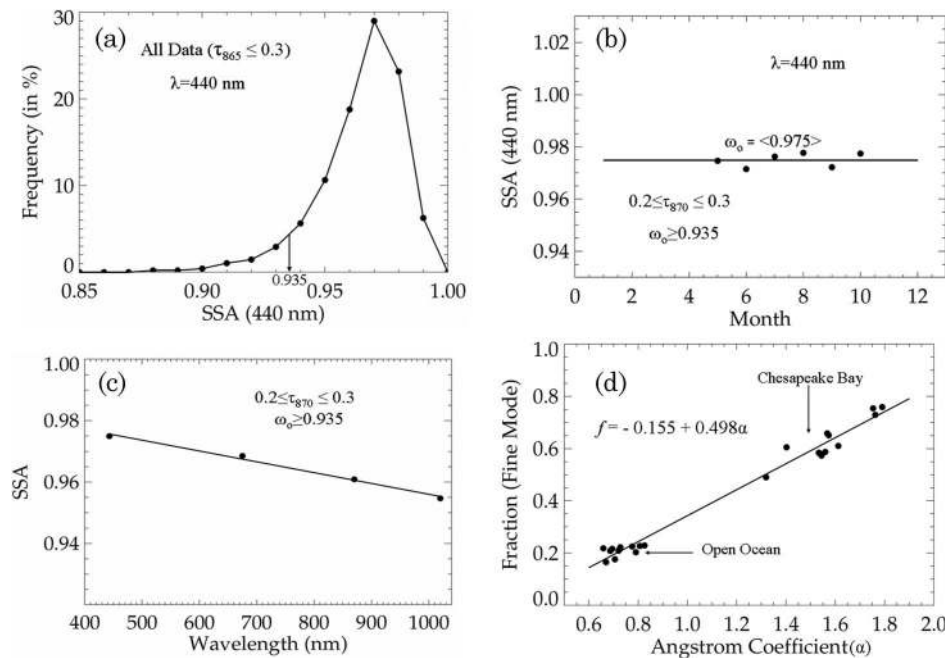


Fig. 3. (a) Frequency distribution of SSA at 440 nm using all observations in the combined dataset of SERC, Wallops Island, and COVE sites. Only 5% of the data have  $\text{SSA} \leq 0.935$ . (b) Monthly mean value of SSA ( $\omega_0$ ) of all observation, where  $0.2 \leq \tau_{870} \leq 0.3$ . The dataset did not have observations for the month of January, February, March, April, November, or December that satisfied the above stated optical thickness criteria. (c) Spectral dependence of SSA ( $\omega_0$ ) of all CBR data where  $0.2 \leq \tau_{870} \leq 0.3$  and  $\omega_0 \geq 0.935$ . (d) Relationship between angstrom coefficient ( $\alpha_{440}$ ) and fraction of fine-mode aerosols.

fine-mode fraction that satisfies both the CBR and open-ocean aerosols. This is shown in Fig. 3(d). The correlation between these quantities is easily explained by the fact that the angstrom coefficient is large when the effective radius of aerosols is small and it decreases as the effective radius of the aerosols increases, while the fine-mode-fraction value is large when the effective radius is small and vice versa. We did not expect, however, that this relationship between angstrom coefficient and fine-mode fraction would be linear.

### 3. Aerosol Models for Satellite Data Reduction

#### A. Size Distributions

In the past, many authors, including Tanre *et al.* [25], Omar *et al.* [26], Gross *et al.* [27], and Zagolski *et al.* [28] have used AERONET data to develop models to retrieve microphysical and optical properties of aerosols from satellite observations. For example, Tanre *et al.* [25] used AERONET data and constructed five models of fine-mode and four models of coarse-mode aerosols, and then used the 20 combinations of the fine and coarse modes to retrieve aerosol properties over the ocean from observations taken by MODIS sensors. Omar *et al.* [26] used cluster analysis techniques to classify all available AERONET data over land and ocean into six categories: desert dust, biomass burning, background rural, polluted continental, marine, and dirty pollution. These six categories are being used to retrieve aerosol properties from the CALIPSO data. Unfortunately, their method yields only one aerosol model for all maritime conditions.

Gross *et al.* [27] used a neural network technique to classify the AERONET data into 64 models. However, they recommend only eight models to process ocean color data from SeaWiFS. Most recently, Zagolski *et al.* [28] proposed an AERONET-based climatology of aerosol models to retrieve oceanic parameters such as chlorophyll concentration and primary productivity. However, they do not suggest any method to account for the seasonal variations in the modal radii of the aerosol distributions, particularly in the coastal regions, such as CBR, as shown in Figs. 2(a) and 2(b).

Below, we describe the details of our new aerosol models to retrieve oceanic parameters, such as chlorophyll concentration and primary productivity, from SeaWiFS and MODIS sensors. Based on the results presented in the preceding section, it seems logical to develop sets of aerosol models where the microphysical and optical properties are simply the monthly mean values of the AERONET data, but this approach is problematic. First, we do not have SSA albedo value for the months of January, February, March, April, November, and December [see Fig. 2(b)]. In addition, although such a suite of models will, on the average, produce reasonable retrievals, the individual retrievals will have large errors because the relative humidity ( $Rh$ ) varies from day to day and often shows large variation. Using data from the National Climate Environment Predictions (NCEP), we find that  $Rh$  over the CBR generally varies from 70% to 80% but, often-times, it drops to almost 40%. On the West Coast of California, the  $Rh$  often drops to 25%–30%. Over the open ocean, the relative humidity generally varies



from 75% to 85%, but it often drops to 65% or increases to 90%. Hänel [13] and SF79 have shown that the radii of the particles both in the fine and coarse mode increase with relative humidity. In general, the rate of increase is larger for  $Rh > 70\%$  and becomes almost exponential beyond  $Rh > 95\%$  (Hänel [13], Wang and Martin [29]). Furthermore, with an increase in relative humidity, the effective value of the refractive index (both real and imaginary) approaches that of water, which is nonabsorbing. Another issue is that the AERONET retrieval algorithm assigns the same value of refractive index (or SSA) to both the fine- and the coarse-mode particles. We believe this is not correct because, over the open ocean and away from the polluted areas, the coarse mode primarily consists of sea salt, which is not absorbing. If we accept that the coarse-mode particles are mostly sea-salt particles, then we must change the refractive index of the fine-mode particles to get the same retrieved SSA.

To develop models of aerosols for coastal and open-ocean conditions, we assumed that the aerosols could be represented by a sum of two lognormal distributions, one representing the fine mode and the other representing the coarse mode. We further assumed that the fine-mode aerosols are continental in nature and the coarse-mode aerosols are oceanic in nature. This means that coarse-mode aerosols are nonabsorbing and all absorption is due to fine-mode particles. We do recognize that, over the open ocean, the fine-mode aerosols will contain significant amounts of non-sea-salt sulfate aerosols, which are nonabsorbing. However, over the open ocean, the fraction of fine-mode aerosol is small ( $\sim 20\%$ ) and the coarse mode ( $\sim 80\%$ ) dominates the scattering process. It should be noted that these fractions are by volume and not by the number of aerosol particles, as was the case for the GW94's ocean and coastal models discussed in Section 1. The exact percentages will vary with  $Rh$ , since the coarse-mode sea-salt particles will grow more with increasing  $Rh$  than will the continental origin, fine-mode particles.

To incorporate the effect of relative humidity on the growth of fine- and coarse-mode aerosols, we followed a method first proposed by Hänel [13] and later used by SF79 to determine the effective refractive index ( $m$ ), and modal radii ( $r_f$  and  $r_c$ ) at a number of  $Rh$  values from 30% to 95%. Hänel's method involves determining the radius as a function of relative  $Rh$  from the wet-to-dry mass ratio, which is given by the following expression (Hänel [13]):

$$r(a_w) = r_o \left[ 1 + \rho \frac{m_w(a_w)}{m_o} \right]^3, \quad (5)$$

where  $a_w$ , called water activity, is the same as  $Rh$  corrected for the curvature of the particle surface,  $r_o$  is the radius of the particle for  $Rh = 0$ ,  $m_o$  is the mass of the dry particle,  $m_w$  is the mass with condensed water, and  $\rho$  is the ratio of wet-to-dry mass density of aerosols. Hänel [13] also provided tabular values for the ratios  $m_w/m_o$  and  $\rho$  for six types of aerosols

for a number of  $Rh$  values varying from 20% to 99%. In this paper, we have assumed that the growth rates of our fine- and coarse-mode aerosols, respectively, are the same as Hänel's tropospheric and maritime aerosols.

Because the AERONET data do not report the  $Rh$  values at the observation sites, we assumed that the monthly average values of modal radii for the fine and coarse modes correspond to the climatological values of  $Rh$  over each site, as determined from NCEP monthly climatologies. This allowed us to determine a dry-mass radius value for every monthly average value of the modal radius. We averaged the dry-mass radius values for the fine and coarse modes and then determined  $r(Rh)$  for a number of  $Rh$  values from 30% to 99% using Hänel's tabulated values for  $\rho$  and  $m_w/m_o$  for tropospheric and maritime aerosols. The results on the variation of modal radius and standard deviation with  $Rh$  for open ocean and CBR are shown in Figs. 4(a)–4(d).

For the modal radius, the agreement between the data and the model results is good, except for coarse mode over open ocean, where, for  $Rh < 75\%$ , the model values are lower than the data. The reverse is seen for  $Rh > 80\%$ . For the standard deviation, the relationship is very noisy. We do not have any model to relate the standard deviation with  $Rh$ , and the least square lines in Figs. 4(c) and 4(d) show weak trends that we find difficult to interpret. We, therefore, used the average value to represent the standard deviation, which essentially makes it independent of  $Rh$ .

#### B. Optical Properties (Refractive Index and Single Scattering Albedo)

The next task in developing the models was to determine the index of refraction such that the predicted value of SSA agrees with observed value and shows similar spectral dependence. Initially we assumed that our fine- and coarse-mode aerosols are the same as SF79's tropospheric and maritime aerosol models. They define their tropospheric aerosols as consisting of a mixture of water-soluble substances, such as ammonium and calcium sulfate (70%), and dustlike aerosols (30%), and maritime aerosols as consisting of sea salts. We used SF79's dry-mass refractive index values and, using the following equation (Hänel [13]), computed the refractive index values for a number of  $Rh$  values from 30% to 95%. The numerical values are reported at the nominal center wavelengths of the SeaWiFS sensor given in Table 3:

$$n = n_w + (n_o - n_w) \left[ \frac{r_o}{r_{rh}} \right]^3, \quad (6)$$

Here, the symbols  $n_w$  and  $n_o$ , respectively, refer to the complex indices of refraction of water and dry aerosols, and  $r_o$  and  $r_{rh}$ , respectively, refer to the radius of the aerosols in the dry state and at  $Rh$ .

To summarize, based on AERONET observations, we constructed bimodal lognormal aerosol size



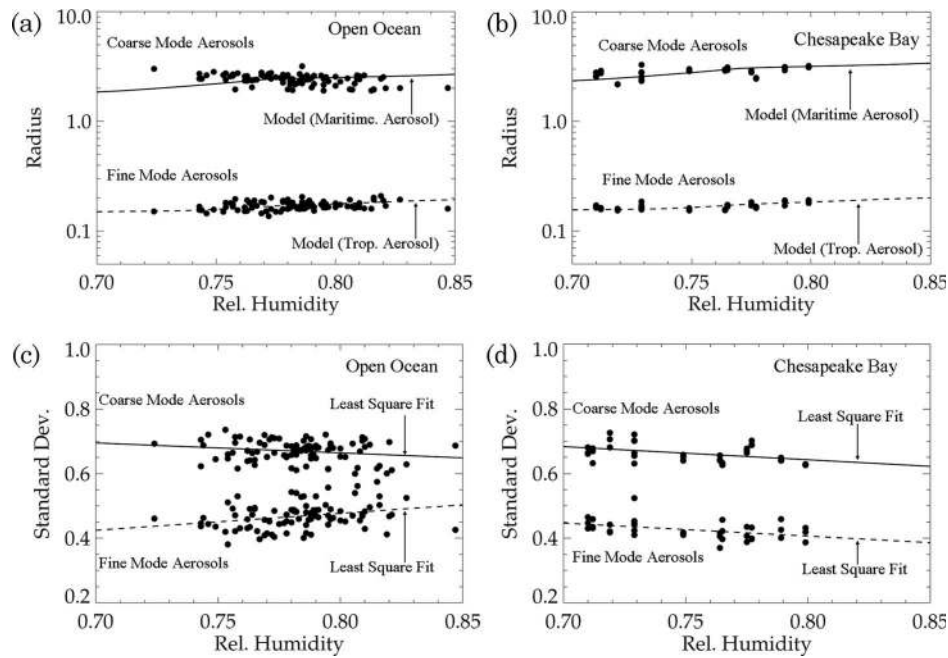


Fig. 4. (a) Growth of fine- and coarse-mode aerosol radius with an increase in  $Rh$  over the open ocean. The symbols represent the monthly mean radius data and the solid and dashed curves represent the model results (Hänel [13]). (b) Same as (a), except for CBR. (c) Change in the standard deviation of fine- and coarse-mode distributions with  $Rh$  over the open ocean. The symbols represent the monthly mean standard deviation values and the solid and dashed curves are the least square fit to the data. (d) Same as (c), except for CBR.

distributions, where the modal radii and refractive index values were explicitly dependent on  $Rh$ . For the purposes of generating lookup tables (LUTs), we considered eight values of  $Rh$  (30%, 50%, 70%, 75%, 80%, 85%, 90%, and 95%). We did not consider  $Rh$  values greater than 95% because, as stated earlier, the modal radius values for both the fine- and the coarse-mode radii increase almost exponentially beyond  $Rh > 95\%$ . The tabular values of the modal radius, standard deviation, and the ratio of the wet-to-dry radius for the fine- and coarse-mode aerosols are given in Table 4. For standard deviation of the bimodal distributions, we used the average value of the monthly means reported in Figs. 4(c) and 4(d). The rationale was that, although there were trends in the data, there was no guiding physics to extend the trend outside the humidity range of the observations. The refractive index values were determined from Eq. (6) using tabular data in Table 3 for  $Rh = 0$  and the wet-to-dry radius ratio given in Table 4.

After selecting the values of modal radii, standard deviations, and refractive indices of the fine and

coarse modes for each humidity value, we constructed ten distributions by varying the fine-mode fraction from zero to 1. In other words, we created 80 distributions to process the satellite data. In this paper, the ten aerosol distributions are referred as  $M_{nn}$ , where  $nn$  represents the aerosol size distribution number. Examples of two such distributions for  $Rh = 50\%$  and  $Rh = 80\%$  are shown in Fig. 5(a). For comparison purposes, we also show, in Fig. 5(b), GW94's [8] coastal and maritime aerosol size distributions for  $Rh = 80\%$ . Note that the standard deviation and modal radius values for the fine and coarse modes, respectively, are larger and smaller than values shown in Fig. 5(a).

To ensure that our models exhibit the same spectral dependence of SSA as observed in Fig. 3(c), we performed the Mie calculations for all the wavelengths of the SeaWiFS sensors, and computed the effective radius and SSA values for the 80 models ( $8Rh \times 10$  fine-mode fraction) described above. Next, we interpolated these values for the relative humidity and effective radius values of the CBR aerosols

Table 3. Complex Refractive Index Values for Different Constituents of the Fine- and Coarse-Mode Aerosols for SeaWiFS Sensor at  $Rh = 0$  (SF79)

Wavelength (nm)	Water Soluble	Dustlike	Sea Salt	Soot	Water
412	1.530 – 3.0050i	1.530 – 3.0080i	1.500 – 3.0000i	1.750 – 3.4586i	1.338 – 3.0000i
443	1.530 – 3.0050i	1.530 – 3.0080i	1.500 – 3.0000i	1.750 – 3.4551i	1.337 – 3.0000i
490	1.530 – 3.0050i	1.530 – 3.0080i	1.500 – 3.0000i	1.750 – 3.4500i	1.335 – 3.0000i
510	1.530 – 3.0050i	1.530 – 3.0080i	1.500 – 3.0000i	1.750 – 3.4500i	1.334 – 3.0000i
555	1.530 – 3.0060i	1.530 – 3.0080i	1.499 – 3.0000i	1.750 – 3.4394i	1.333 – 3.0000i
670	1.530 – 3.0066i	1.530 – 3.0080i	1.490 – 3.0000i	1.750 – 3.4300i	1.331 – 3.0000i
765	1.526 – 3.0091i	1.526 – 3.0080i	1.486 – 3.0000i	1.750 – 3.4300i	1.330 – 3.0000i
865	1.520 – 3.0121i	1.520 – 3.0080i	1.480 – 3.0000i	1.750 – 3.4303i	1.329 – 3.0000i

**Table 4. Modal Radii ( $r_{vf}$ ,  $r_{vc}$ ), Standard Deviations ( $\sigma_f$ ,  $\sigma_c$ ), and Ratios of Wet-to-Dry Aerosol Radius ( $r_{vf}/r_{ovf}$ ,  $r_{vc}/r_{ovc}$ ) for Eight Values of Relative Humidity Used in This Study<sup>a</sup>**

$Rh$	$r_{vf}$	$\sigma_f$	$r_{vc}$	$\sigma_c$	$r_{vf}/r_{ovf}$	$r_{vc}/r_{ovc}$
0.30	0.150	0.437	2.441	0.672	1.006	1.009
0.50	0.152	0.437	2.477	0.672	1.019	1.024
0.70	0.158	0.437	2.927	0.672	1.063	1.210
0.75	0.167	0.437	3.481	0.672	1.118	1.439
0.80	0.187	0.437	3.966	0.672	1.255	1.639
0.85	0.204	0.437	4.243	0.672	1.371	1.753
0.90	0.221	0.437	4.638	0.672	1.486	1.917
0.95	0.246	0.437	5.549	0.672	1.648	2.293

<sup>a</sup>The subscripts  $v$ ,  $f$ , and  $c$ , respectively, refer to volume space, fine mode, and coarse mode of the aerosols

described in Fig. 3(c). An example of the comparison for the month of September is shown in Fig. 6(a). What we find is that our predicted SSA between 700 and 900 nm drops off much faster than that observed in the AERONET data. The results for other months were similar. We attribute the sharp drop in calculated SSA to an increase in the value of the imaginary part of the refractive index of the water-soluble aerosols that constituted 70% of the fine-mode aerosols. We also noted that the real part of refractive index for water-soluble and dustlike aerosols were essentially the same in the visible and near-IR part of the spectrum. Also, in the same part of the spectrum, the imaginary part of the dustlike aerosols were almost constant and were a little higher than for water-soluble aerosols. Based on these observations, we varied the composition of the fine-mode aerosols and found that a mixture of 99.5% of dustlike aerosols and 0.5% of soot gave a reasonably good agreement with the AERONET data. An example for the month of September is shown in Fig. 6(b). Results for other months were very similar, except for the month of October, where the predicted values of SSA at all wavelengths were lower by  $\sim 1\%$ .

#### 4. Impact of New Models on Satellite Ocean Color and Aerosol Retrievals

To evaluate the impact of the aerosol model changes on satellite sensor retrievals of aerosol optical thickness,  $\tau$ , and water-leaving radiance,  $L_w$ , we incorporated the new models into the operational version of NASA's ocean color processing code, 12 gen. The operational code uses the GW94 algorithm to deter-

mine the aerosol contributions, and it employs an iterative bio-optical model (Bailey *et al.* [30]) to separate the aerosol and water signals in complex turbid waters. Implementation of the new models within the NASA code was achieved through generation of a new set of LUTs to replace the standard SF79 LUTs. The new LUTs were created with the current version of Ahmad and Fraser's vector radiative transfer code [31] for the ocean-atmosphere system.

Although we did not change the operational processing algorithm of GW94, use of the new tables required that we assign an  $Rh$  value to each instantaneous field of view (IFOV). The concept is to select two  $Rh$  values from the LUTs that bracket the IFOV value and, for each  $Rh$  value, use its ten aerosol models to compute aerosol reflectance ( $\rho_{a\lambda}$ ) at all wavelengths ( $\lambda$ ), and then use the weighted sum to determine the best estimates of aerosol reflectance.

Initial processing of the SeaWiFS data showed a significant frequency of cases where scaled reflectance  $\epsilon_{765} (= \rho_{a765}/\rho_{a865})$ , as determined from the satellite data, was below the range of values in the LUTs. This suggested that the sensor was sometimes observing aerosol size distributions with larger particles than the mean observations measured at the open-ocean AERONET sites. To ensure that the model size distributions spanned the full range of the satellite observations, we decided to increase the oceanic coarse-mode radius ( $r_{vc}$ ) by  $3\sigma$ , where  $\sigma$  is the standard deviation of the monthly mean of the coarse-mode AERONET oceanic data. This allowed the models  $\epsilon_{765}$  values to span the range of observed  $\epsilon_{765}$ . The revised values of  $r_{vc}$  are given in Table 4.

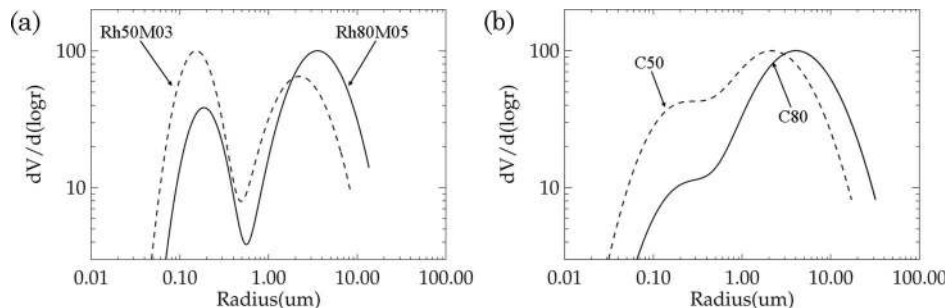


**Fig. 5.** (a) Examples of the new size distributions (Rh80M02 and Rh80M05). Both distributions are normalized to a value of 100 at their respective maxima. (b) Examples of two SF79 aerosol size distributions. C50 and C80 refer to coastal aerosol distributions for  $Rh$  of 50% and 80%, respectively.

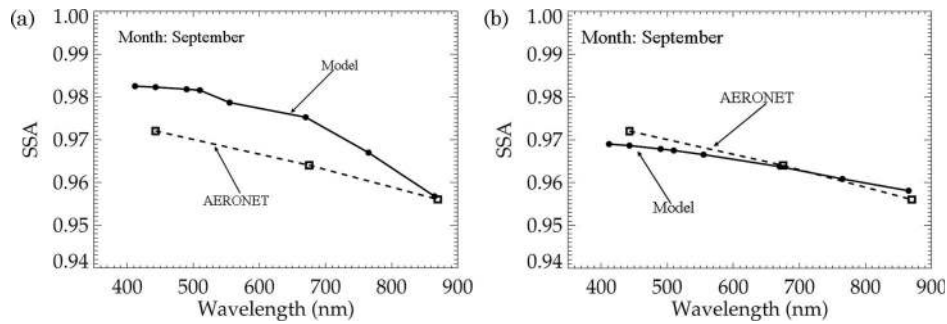


Fig. 6. (a) Comparison of spectral dependence of SSA as reported by AERONET for  $\tau_{870} \leq 0.3$ , and as predicted by our model where the fine mode consists of 70% water-soluble and 30% dustlike aerosols. (b) Same as in (a), except the fine mode consists of 99.5% dustlike aerosols and 0.5% soot aerosols.

Using the aerosol model LUTs derived from Table 4, we processed a subset of the SeaWiFS mission consisting of full global area coverage for every eighth 4-day period spanning the period from late 1997 through 2009. To further isolate the effect of aerosol model change and associated  $Rh$ -based model selection, we also updated the vicarious calibration using the standard approach outlined in Franz *et al.* [32]. This has the effect of altering the 765 nm calibration to force the mean angstrom coefficient retrieval at the South Pacific Gyre (SPG) to be the same for both the old and new model suites. The water-leaving radiances were then recalibrated against the MOBY in-water buoy using the vicariously calibrated aerosol reflectance retrievals.

The results of this processing test are shown in Figs. 7(a) and 7(b), where results are plotted as a function of time for all data collected over deep-ocean

water (depth greater than 1000 m). Figure 7(a) shows that  $\tau_{865}$  values retrieved from the new models are lower than those retrieved from old models. The mission-average value of  $\tau_{865}$  retrieved over deep ocean from the new aerosol models is  $0.100 \pm 0.004$ , which is close to the average AERONET value for  $\tau_{870}$  of  $0.086 \pm 0.066$ , for the eight open-ocean sites used in this study. The average value of  $\tau_{865}$  retrieved using the old models is  $0.131 \pm 0.005$ . Figure 7(b) shows a temporal trend comparison of  $L_{wn}$  for the 412, 490, and 555 nm bands of SeaWiFS, averaged over all deep-water retrievals. Note that  $L_{wn}$  is simply equal to  $L_w(F_o/E_d)$ , where  $F_o$  and  $E_d$  are, respectively, the solar irradiance at the top and bottom of the atmosphere. The results show that the retrieved  $L_{wn}$  values from the two sets of aerosol models (old and new) over the same region of the deep ocean are essentially the same. In the blue bands at 412

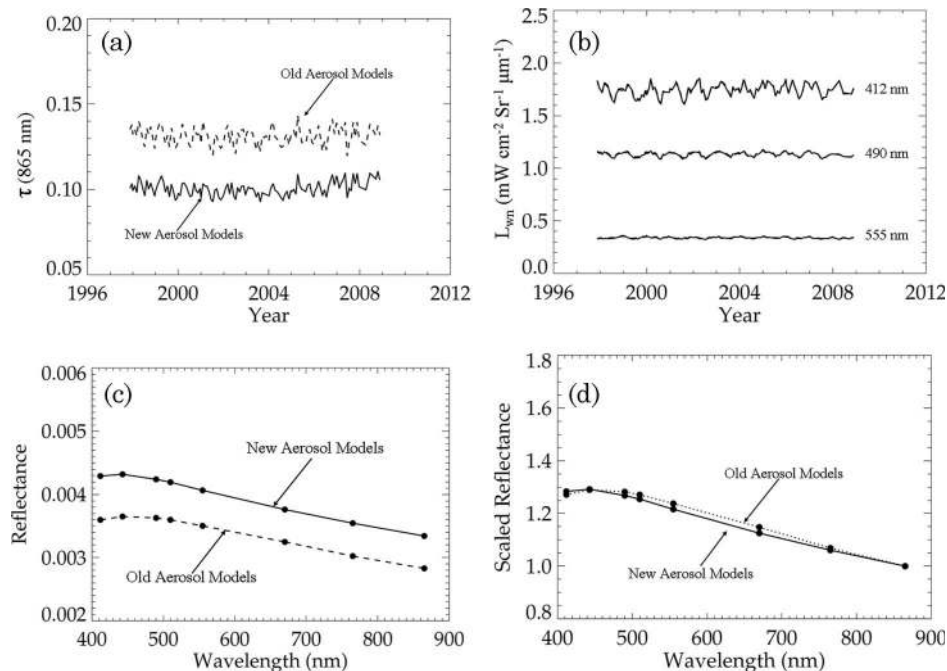


Fig. 7. (a) Ten-year time series of  $\tau_{865}$  over deep ocean derived from SeaWiFS sensor using new and old aerosol models. (b) Ten-year time series of normalized water-leaving radiances,  $L_{wn}$ , over deep ocean derived from SeaWiFS sensors using new and old aerosol models. (c) TOA reflectance computed from old (M70) and new (Rh80M06) aerosol models. The input parameters were  $\theta_0 = 30^\circ$ ,  $\theta = 42^\circ$ ,  $\phi = 120^\circ$ , and  $\tau = 0.1$  (d) Same as (c), except that the reflectances for each aerosol model were normalized by their respective value for the 865 nm band.



and 490 nm, the new (old) values of  $L_{un}$  are, respectively,  $1.744 \pm 0.056$  and  $1.557 \pm 0.041$  ( $1.750 \pm 0.056$  and  $1.566 \pm 0.041$ )  $\text{mW}/\text{cm}^2/\text{Sr}/\mu\text{m}$ , and in the green band at 555 nm, the value is  $0.338 \pm 0.008$  ( $0.342 \pm 0.007$ )  $\text{mW}/\text{cm}^2/\text{Sr}/\mu\text{m}$ .

The results in Fig. 7(a) can be explained. We know that, at small aerosol optical thickness values, the single scattering phenomenon dominates the scattering process and, aside from constant terms involving solar irradiance and the cosine of solar and sensor view angles, the aerosol reflectance is essentially a product of SSA ( $\omega_o$ ), phase function ( $p$ ), and aerosol optical thickness ( $\tau$ ). If we look at Figs. 5(a) and 5(b), we find that the size distributions of the old models are broad and contain more large particles than the new distributions. Since large particles have small values of phase function in the backward direction, the old models will retrieve a larger value of optical thickness than the new models, and this is what we see in Fig. 7(a).

The results in Fig. 7(b) are more intriguing. In spite of large differences in aerosol optical thickness [see Fig. 7(a)], the differences in water-leaving radiances are very small ( $\pm 1\%$  for the 412 and 490 nm bands and  $\pm 3\%$  for 555 nm). This result is, in part, due to the vicarious calibration, which forces the retrieved water-leaving radiances near Lanai, Hawaii to agree, on average, with the MOBY *in situ* radiometric buoy (Franz *et al.* [32]). To understand the results in Fig. 7(b) further, we again consider the single scattering formalism. Here, the most important thing to recognize is that the aerosol reflectance, and, thus, the atmospheric correction, does not depend on the spectral dependence of individual parameters ( $\tau$ ,  $p$ , and  $\omega_o$ ), but on the spectral dependence of the product of parameters  $\tau$ ,  $p$ , and  $\omega_o$ , which, apart from a constant, is the same as reflectance. In other words, two aerosol models with different values of  $\tau$ ,  $p$ , and  $\omega_o$ , and, hence, different reflectance values, can have very similar spectral dependence. We show an example of this in Fig. 7(c), where the two curves show the spectral dependence of TOA reflectance for two aerosol models, M70 (old model) and Rh80M06 (new model). If we compute the reflectance for an aerosol optical thickness of 0.1, we will find that the two models yield completely different values, yet these values show very similar spectral dependence. In fact, if we scale the reflectance values for the two models by their respective values at 865 nm, the resulting curves are nearly identical. This is shown in Fig. 7(d). At present it is difficult to say under what conditions two aerosol models would show similar spectral dependence, but indications are that, if the aerosols are nonabsorbing or weakly absorbing and have very similar angstrom coefficients and  $\epsilon_{765}$  values, then they will show very similar spectral dependence.

We emphasize again that this initial test was designed to yield similar angstrom coefficients at the SPG for both the old and new models, due to the method employed to vicariously calibrate the satel-

lite retrievals (Franz *et al.* [32]). Specifically, we targeted the calibration in the SPG to yield  $\alpha_{510} = 0.2$ , which was based on the idea that aerosols over the SPG are predominately maritime in origin, and the old SF79 maritime model at 90% humidity provided an angstrom of 0.2. Given that the new aerosol models are designed to match AERONET size distributions, it is now appropriate to change the vicarious calibration to directly target AERONET retrievals. The vicarious calibration for SeaWiFS was, therefore, revised to match the mean angstrom coefficient observed at the Tahiti AERONET site (nearest to the SPG), which is approximately  $\alpha_{440} = 0.68$ . Relative to the initial processing results using the new models, this change in calibration, followed by an associated recalibration of the visible bands to MOBY, again resulted in only a minor change to the water-leaving radiance retrievals (2%–3% decrease) over deep-ocean waters. The mean deep-water  $\alpha_{510}$ , however, increased from 0.3 to 0.7, while the  $\tau_{865}$  retrievals decreased by only 4%.

## 5. Application to Ocean Color Reprocessing and Assessment of Results

The new aerosol models and  $Rh$ -based model selection scheme were incorporated into NASA's operational ocean color processing code in preparation for SeaWiFS reprocessing. This update included the revised vicarious calibration based on the AERONET measurements at Tahiti, as well as a host of other changes to the processing algorithms that are beyond the scope of this manuscript, but which have little effect on the aerosol retrievals. Here, we compare the reprocessing results for  $\tau_{865}$  and  $\alpha_{443}$  with AERONET measurements of  $\tau_{870}$  and  $\alpha_{440}$  over two sites: Bermuda and Chesapeake Bay (Wallops Island) that, respectively, represent open-ocean and coastal waters. To minimize the large statistical fluctuations in the individual match-up values, we utilized the monthly mean values of  $\tau$  and  $\alpha$  for comparison. This approach allows us to use all available retrievals for the comparison, and better reveal the true aerosol properties.

To create the match-up database, a box of  $\pm 0.25$  degrees in latitude and longitude was constructed around the AERONET site while ensuring that the entire box was over the ocean. For the satellite, 1 km resolution (MLAC) Level 2 daily SeaWiFS data were selected and quality screened following the protocols in Bailey and Werdell [33]. For the AERONET data, the Level 2 daily averaged products of direct Sun measurements were used. The Level 2 product satisfies all the quality control criteria, including thin clouds in the field of view.

The results on the comparison of optical thickness over Bermuda and Wallops Island for the period shown in Table 1 are, respectively, shown in Figs. 8(a) and 8(b). The numbers of matchups are 53 and 94. The solid line is the 1:1 line and the dashed lines represent the  $\pm 0.02$  uncertainty in the retrieved optical thickness. The uncertainty of  $\pm 0.02$  is considered a desired goal of retrieving aerosol optical thickness from



satellite measurements (Mishchenko *et al.* [34]). We find the agreement between the satellite retrievals of  $\tau_{865}$  and AERONET measurements of  $\tau_{870}$  to be good, with 81% of the data over Bermuda and 78% of the data over Wallops Island falling within the desired uncertainty of  $\pm 0.02$ . The bias and rms error statistics for Bermuda (Wallops Island) are, respectively, 0.010 (−0.009) and 0.002 (0.002). Time series of optical thickness over the two sites, for both SeaWiFS (using the new aerosol models) and AERONET are shown in Figs. 8(c) and 8(d). For comparison purposes, we also show the time series for SeaWiFS as determined from the old aerosol models. It is apparent that the optical thicknesses derived from the new aerosol models are in better agreement with the AERONET observations than those obtained from the old models. Although

the old models do show the same trend, the magnitude of retrieved optical thickness is higher than that observed in the AERONET data. This observation is consistent with the conclusions of Wang *et al.* [15] that the SF79 models overestimate the aerosol optical thickness over the ocean. It is interesting to note that, over Wallops Island, the new models faithfully capture the magnitude as well as the trend in optical thickness.

We also compared the  $\alpha_{443}$  retrieved from SeaWiFS using the new models with  $\alpha_{440}$  from AERONET. A time series of angstrom coefficient for each site is shown in Figs. 8(e) and 8(f). For comparison purposes, we also show the time series of  $\alpha_{443}$  retrieved from the old models. Again, we find that the results from the new aerosol models are in very good agreement with AERONET. The average value of  $\alpha_{443}$  from

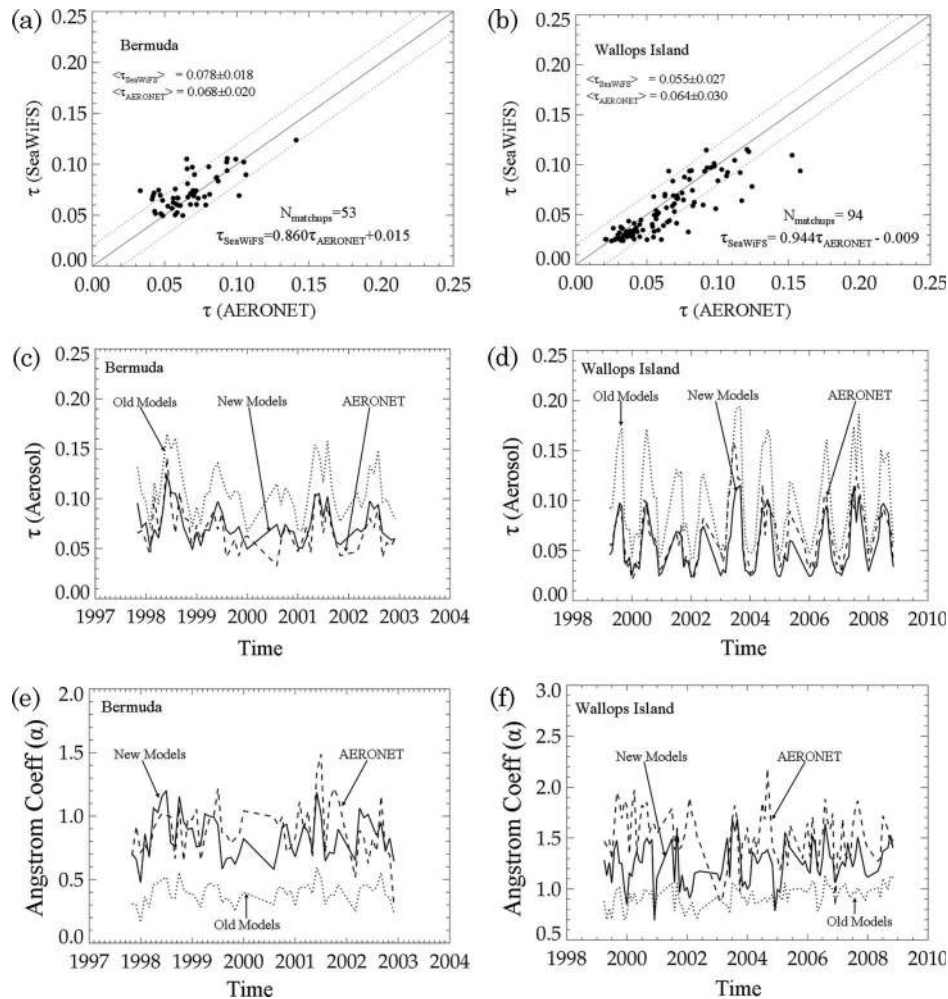


Fig. 8. (a) Scatter plot of SeaWiFS versus AERONET monthly mean aerosol optical thickness ( $\tau$ ) over Bermuda. The solid curve is a 1:1 curve and the dotted curves represent  $\pm 0.02$  change in  $\tau$  from the 1:1 curve. Approximately 81% of the data are within the dotted curves. The robust least squares fit equation is  $\tau_{\text{SeaWiFS}} = 0.860 \tau_{\text{AERONET}} + 0.015$ , and bias and rms statistics are, respectively, 0.010 and 0.002. (b) Same as in (a), except that 78% of the data are within the dotted curves. The robust least squares fit equation is  $\tau_{\text{SeaWiFS}} = 0.944 \tau_{\text{AERONET}} - 0.005$ , and the bias and rms statistics are, respectively, −0.009 and 0.002. (c) Time series of monthly mean aerosol optical thickness ( $\tau_{865}$ ) over Bermuda derived from the old and the new models as well as from AERONET sunphotometer. Note that  $\tau$  values derived from the new models are much closer to AERONET than those derived from the old models. (d) Same as (c), except that the data were taken over Wallops Island. (e) Time series of monthly mean angstrom coefficient ( $\alpha_{443}$ ) over Bermuda derived from the old and the new models as well as from the AERONET sunphotometer. Note that  $\alpha$  values derived from the new models are much closer to AERONET than those derived from the old models. (f) Same as (e), except that the data were taken over Wallops Island. The AERONET values are slightly larger than those retrieved from the new models.

the new models is  $0.841 \pm 0.171$  and from AERONET is  $0.891 \pm 0.211$ . The average value of  $\alpha_{443}$  from the old models is  $0.394 \pm 0.087$ , which is significantly lower than AERONET value.

## 6. Summary and Conclusions

In this paper, we have described the development of a new suite of aerosol models to reduce the satellite data from the SeaWiFS and MODIS sensors and retrieve aerosol optical thickness ( $\tau$ ), angstrom coefficient ( $\alpha$ ), and the water-leaving radiances ( $L_w$ ) originating from the sub-surface of the ocean. The latter is needed to quantify phytoplankton chlorophyll-a, CDOM, and primary productivity of the ocean. There was an urgent need for new aerosol models because the old models used by the OBPG until recently were based on SF79 models that were developed for climate and radiation studies and it was found that, over the ocean, the old models consistently overestimated  $\tau$  and underestimated  $\alpha$ .

To develop the suite of new aerosol models, we considered a number of oceanic and coastal AERONET sites and selected eight sites over open ocean and three sites over the CBR. We used the CBR as a proxy for the coastal waters because it is highly turbid in the north and nearly oceanic in the south, and aerosols over this region are influenced by industrial and city pollutions, agricultural land use, and the Atlantic Ocean. We analyzed the open-ocean and CBR data separately. To get a better understanding of the variation in aerosol microphysical and optical properties, we converted the daily averaged data into monthly averages and examined in detail the seasonal behavior of a few selected parameters, including mean geometric modal radius (in  $dV/d(\ln r)$  space), standard deviations, effective radius, and relative concentration of fine- and coarse-mode particles. We found that, over the CBR, both the fine- and coarse-mode particle size distributions showed a strong seasonal dependence, with maximum modal values in the summer time; however, the standard deviation values were relatively constant. Over the open-ocean, modal radii showed a weak seasonal dependence and the standard deviation values were noisy and did not show any seasonal dependence.

We also found that the seasonal variability of the modal radii ( $r$ ) of the fine- and coarse-mode aerosols was correlated with  $Rh$ , and that this correlation was consistent with Hänel's model [13] of growth of particle radius with  $Rh$ .

Using AERONET retrievals as a guide, we constructed a set of bimodal lognormal aerosol size distributions, where the modal radius and refractive index values were explicitly dependent on  $Rh$ . For standard deviation, we decided to use the average value of all the monthly means. The rationale was that, although there was a trend in the data, there was no guiding physics to extend the trend outside the humidity range of the observations.

After defining the details of the modal radii, standard deviations, and refractive indices of the fine and

coarse modes, we constructed ten distributions (for each relative humidity value) by varying the fine-mode fraction from zero to 1. In all, we created 80 distributions ( $8Rh \times 10$  fine-mode fraction) to process the satellite data. Also, to ensure that our new models exhibited the same spectral dependence of SSA as observed in the AERONET data, we varied the composition of the fine-mode aerosols and found that a mixture of 99.5% of dustlike aerosols and 0.5% of soot gave a reasonably good agreement (approximately  $\pm 1\%$ ) with the AERONET data.

Initially, we processed a subset of the SeaWiFS mission data using both the new and old aerosol models and retrieved aerosol optical thickness,  $\tau$ , angstrom coefficient,  $\alpha$ , and water-leaving radiance,  $L_w$ , over the ocean. We found that the average  $\tau_{865}$  value over deep ocean using the new aerosol models was  $0.100 \pm 0.004$ , whereas the average  $\tau_{870}$  value from AERONET for the eight open-ocean sites used in this study was  $0.086 \pm 0.066$ . The  $\tau_{865}$  value from old models was  $0.131 \pm 0.005$ , which was substantially higher than the AERONET value. In contrast, the retrieved normalized water-leaving radiance,  $L_{wn}$ , from the new and the old sets of aerosol models over the deep ocean changed by only a few percent. In the blue band at 412 nm, the new (old) values of  $L_{wn}$  were  $1.744 \pm 0.056$  ( $1.750 \pm 0.056$ ) mW/cm<sup>2</sup>/Sr/μm, and in the green band at 555 nm, the new (old) values of  $L_{wn}$  were  $0.338 \pm 0.008$  ( $0.342 \pm 0.007$ ) mW/cm<sup>2</sup>/Sr/μm.

The fact that the  $\tau_{865}$  retrieved values from the new models are smaller than from the old models can be easily explained by noting that the old aerosol models are broad (large standard deviation) and have more large particles in them than the new models. Since large particles scatter less in the backward direction, the old models having smaller values of phase function ( $p$ ) in the backward direction would yield larger values of aerosol optical thickness than the new models.

Also, we believe that the changes in the  $L_{wn}$  are small partly due to the approach employed for vicariously calibrating the water-leaving radiance retrievals, and because the new and old models can produce very similar spectral dependence. This can be further explained in the following way. We know that for a given set of radiance measurements, the inversion theory (i.e., retrieval of size distribution from a set of radiance measurements) does not guarantee a unique solution; rather, it admits many solutions. Therefore, it is not surprising that two sets of aerosol distributions would yield the same atmospheric correction and, hence, the same values of  $L_{wn}$ . In addition, the most important thing to recognize is that the atmospheric correction does not depend on the spectral dependence of individual parameters ( $\tau$ ,  $p$ , and  $\omega_o$ ), but rather depends on the spectral dependence of scaled reflectance  $\epsilon_\lambda (= \rho_{a\lambda}/\rho_{a865})$ . In other words, two aerosol size distributions with different modal radii and standard deviations can have very similar spectral dependence of  $\epsilon_\lambda$  and, hence, very similar atmospheric correction. An example of this is

shown in Fig. 7(d). At present it is difficult to say under what conditions two aerosol models would show similar spectral dependence. However, it appears that, if the aerosols are nonabsorbing or weakly absorbing and have very similar angstrom coefficients and very close  $\epsilon_{765} (= \rho_{a765} - \rho_{a865})$  values, that is, the reflectances have the same spectral trend over 765 to 865 nm, then they will most likely show very similar spectral dependence and, hence, similar atmospheric correction.

As a part of error analysis, we found that the reflectance measurements in the 765 and 865 bands of SeaWiFS essentially define the coarse mode of the distribution, whereas, the  $\epsilon_{765}$  value, which is the ratio of  $\rho_{a765}/\rho_{a865}$ , locks the relative weights of the fine and coarse modes. Hence, the error in reflectance values,  $\rho_{a\lambda}$ , at a shorter wavelength (blue or green part of the spectrum) would depend on the modal radius ( $r_{vf}$ ) and standard deviation ( $\sigma_f$ ) of the fine mode. In reality, any change in the values of these two parameters will also affect the computed  $\epsilon_{765}$ . The magnitude would depend on the sensitivity of  $\epsilon_{765}$  on  $r_{vf}$  and  $\sigma_f$ .

Finally, we showed the aerosol optical thickness and angstrom coefficients retrieved for SeaWiFS using the new aerosol models and the revised vicarious calibration are now in very good agreement with AERONET measurements. We demonstrated that 81% of SeaWiFS  $\tau_{865}$  retrievals over Bermuda and 78% of the  $\tau_{865}$  retrievals over Wallops Island agree with AERONET to within an uncertainty of  $\pm 0.02$ . The average value of  $\alpha_{443}$  from the new models over Bermuda is  $0.841 \pm 0.171$ , which is in good agreement with the AERONET  $\alpha_{440}$  value of  $0.891 \pm 0.211$ . The average value of  $\alpha_{443}$  from the old models was  $0.394 \pm 0.087$ , which is significantly lower than the AERONET value.

We would like to thank Bo-Cai Gao of the Naval Research Laboratory (NRL) and Suraiya P. Ahmad of INNOVIM for many useful discussions and suggestions, and the members of OBPB, in particular, W. D. Robinson, for providing meteorological data for the analysis of AERONET observations. Also, we thank AERONET staff for maintaining and providing the sunphotometer data used in this study. In addition, we would like to thank two anonymous reviewers for their helpful comments. Eric P. Shettle's work was supported by a grant from NASA's Office of Earth Science and by NRL internal funding [from the Office of Naval Research (ONR)].

## References

1. R. B. Husar, J. M. Prospero, and L. L. Stowe, "Characterization of tropospheric aerosols over the oceans with the NOAA advanced very high resolution radiometer optical thickness operational product," *J. Geophys. Res.* **102**, 16889–16909 (1997).
2. E. P. Shettle and R. W. Fenn, "Models for the aerosols of the lower atmosphere and the effects of humidity variations on their optical properties," AFGL-TR 790214, U. S. Air Force Laboratory, Hanscom Air Force Base, Mass. (1979).
3. G. A. d'Almeida, P. Koepke, and E. P. Shettle, *Atmospheric Aerosols Global Climatology and Radiative Characteristics* (A. Deepak, 1991).
4. C. E. Junge, "Our knowledge on the physico-chemistry of aerosols in the undisturbed marine environment," *J. Geophys. Res.* **77**, 5183–5200 (1972).
5. D. Deirmendjian, "Scattering and polarization properties of water clouds and hazes in the visible and infrared," *Appl. Opt.* **3**, 187–196 (1964).
6. D. Deirmendjian, *Electromagnetic Scattering on Spherical Polydispersions* (Elsevier, 1969).
7. C. N. Davies, "Size distribution of atmospheric particles," *J. Aerosol Sci.* **5**, 293–300 (1974).
8. H. R. Gordon and M. Wang, "Retrieval of water leaving radiance and aerosol optical thickness over the oceans with SeaWiFS: a preliminary algorithm," *Appl. Opt.* **33**, 443–452 (1994).
9. H. R. Gordon, "Atmospheric correction of ocean color imagery in the Earth Observing system era," *J. Geophys. Res.* **102**, 17081–17106 (1997).
10. D. Antoine and A. Morel, "A multiple scattering algorithm for atmospheric correction of remotely sensed ocean color (MERIS instrument): principle and implementation for atmospheres carrying various aerosols including absorbing ones," *Int. J. Remote Sens.* **20**, 1875–1916 (1999).
11. World Climate Program, WCP-112, "A preliminary cloudless standard atmosphere for radiation computation," WMO/TD No. 24, World Meteorological Organization (1986).
12. L. Schutz, "Long-range transport of desert dust with special emphasis on the Sahara," *Ann. N.Y. Acad. Sci.* **338**, 515–532 (1980).
13. G. Hänel, "The properties of atmospheric aerosol particles as functions of the relative humidity at thermodynamic equilibrium with the surrounding moist air," in *Advances in Geophysics*, H. E. Landsberg and J. V. Miehem, eds. (Academic, 1976), Vol. 19.
14. A. Smirnov, B. Holben, Y. J. Kaufman, O. Dubovik, T. F. Eck, I. Slutsker, C. Pietras, and R. N. Halthore, "Optical properties of atmospheric aerosol in marine environments," *J. Atmos. Sci.* **59**, 501–523 (2002).
15. M. Wang, K. D. Knobelspiesse, and C. R. McCain, "Study of the Sea-Viewing Wide Field-of-View Sensor (SeaWiFS) aerosol optical property data over ocean in combination with ocean color products," *J. Geophys. Res.* **110**, doi:10.1029/2004JD004950 (2005).
16. B. N. Holben, T. F. Eck, I. Slutsker, D. Tanre, J. P. Buis, A. Setzer, E. Vermote, J. A. Reagan, Y. Kaufman, T. Nakajima, F. Lavenue, I. Jankowiak, and A. Smirnov, "AERONET—A federated instrument network and data archive for aerosol characterization," *Remote Sens. Environ.* **66**, 1–16 (1998).
17. B. N. Holben, D. Tanre, A. Smirnov, T. F. Eck, I. Slutsker, N. Abuhassan, W. W. Newcomb, J. Schafer, B. Chatenet, F. Lavenue, Y. J. Kaufman, J. VandeCastle, A. Setzer, B. Markham, D. Clark, R. Frouin, R. Halthore, A. Karnieli, N. T. O'Neill, C. Pietras, R. T. Pinker, K. Voss, and G. Zibordi, "An emerging ground-based aerosol climatology: aerosol optical depth from AERONET," *J. Geophys. Res.* **106**, 12067–12097 (2001).
18. O. Dubovik and M. D. King, "A flexible inversion algorithm for retrieval of aerosol optical properties from Sun and sky radiance measurements," *J. Geophys. Res.* **105**, 20673–20696 (2000).
19. O. Dubovik, A. Smirnov, B. Holben, M. D. King, Y. J. Kaufman, T. F. Eck, and I. Slutsker, "Accuracy assessments of aerosol optical properties retrieved from AERONET Sun and sky radiance measurements," *J. Geophys. Res.* **105**, 9791–9806 (2000).
20. O. Dubovik, B. Holben, T. F. Eck, A. Smirnov, Y. J. Kaufman, M. D. King, D. Tanre, and I. Slutsker, "Variability of

- absorption and optical properties of key aerosol types observed in worldwide locations," *J. Atmos. Sci.* **59**, 590–608 (2002).
21. O. Dubovik, "Optimization of numerical inversion in photopolarimetric remote sensing," in *Photopolarimetry in Remote Sensing*, G. Videen, Y. Yatskiv, and M. Mishchenko, eds. (Kluwer Academic, 2004), pp. 65–106.
22. O. Dubovik, A. Sinyuk, T. Lapyonok, B. N. Holben, M. Mishchenko, P. Yang, T. F. Eck, H. Volten, O. Munoz, B. Veihelmann, W. J. vander Zande, J.-F. Leon, M. Sorokin, and I. Slutsker, "Application of spheroid models to account for aerosol particle nonsphericity in remote sensing of desert dust," *J. Geophys. Res.* **111**, D11208, doi:10.1029/2005JD006619 (2006).
23. A. Sinyuk, O. Dubovik, B. Holben, T. F. Eck, F.-M. Breon, J. Martonchik, R. Kahn, D. J. Diner, E. F. Vermote, J.-C. Roger, T. Lapyonok, and I. Slutsker, "Simultaneous retrieval of aerosol and surface properties from a combination of AERONET and satellite," *Remote Sens. Environ.* **107**, 90–108, doi:10.1016/j.rse.2006.07.022 (2007).
24. J. E. Hansen and L. D. Travis, "Light scattering in planetary atmospheres," *Space Sci. Rev.* **16**, 527–610 (1974).
25. D. Tanre, Y. J. Kaufman, and S. Mattoo, "Remote sensing of aerosol properties over oceans using MODIS/EOS spectral radiances," *J. Geophys. Res.* **102**, 16971–16988 (1997).
26. A. H. Omar, J. Won, D. M. Winker, S. Yoon, O. Dubovik, and M. P. McCormick, "Development of global aerosol models using cluster analysis of AERONET measurements," *J. Geophys. Res.* **110**, D10S14, doi:10.1029/2004JD004874 (2005).
27. L. Gross, R. Frouin, C. Pietras, and G. Fargion, "Non-supervised classification of aerosol mixtures for ocean color remote sensing," *Proc. SPIE* **4892**, 95–104 (2003).
28. F. Zagolski, R. Santer, and Q. Aznay, "A new climatology for atmospheric correction based on aerosol inherent optical properties," *J. Geophys. Res.* **112**, D14208, doi:10.1029/2006JD007496 (2007).
29. J. Wang and S. T. Martin, "Satellite characterization of urban aerosols: importance of including hygroscopicity and mixing state in the retrieval algorithms," *J. Geophys. Res.* **112**, D17203, doi:10.1029/2006JD008078 (2007).
30. S. W. Bailey, B. A. Franz, and P. J. Werdell, "Estimation of near-infrared water-leaving reflectance for satellite ocean color data processing," *Opt. Express* **18**, 7521–7527 (2010).
31. Z. Ahmad and R. S. Fraser, "An iterative radiative transfer code for ocean-atmosphere system," *J. Atmos. Sci.* **39**, 656–665 (1982).
32. B. A. Franz, S. W. Bailey, P. J. Werdell, and C. R. McClain, "Sensor-independent approach to vicarious calibration of satellite ocean color radiometry," *Appl. Opt.* **46**, 5068–5082 (2007).
33. S. W. Bailey and P. J. Werdell, "A multi-sensor approach for the on-orbit validation of ocean color satellite data products," *Remote Sens. Environ.* **102**, 12–23 (2006).
34. M. I. Mishchenko, B. Cairns, J. E. Hansen, L. D. Travis, R. Burg, Y. J. Kaufman, J. V. Martin, and E. P. Shettle, "Monitoring of aerosol forcing of climate from space: analysis of measurements requirement," *J. Quant. Spectrosc. Radiat. Transfer* **88**, 149–161 (2004).